Physica B 730 (2026) 418479

Contents lists available at ScienceDirect

Physica B: Condensed Matter

journal homepage: www.elsevier.com/locate/physb

Experiment and simulation in silicon PN-junction photodetectors: Insights into electrical and optical transport

Mohammed Khaouani [a,b], Andrea Sessa [c,*], Sebastiano De Stefano [c], Hichem Rouigueb [d], Mohammed Anes Belbachir [d], Adolfo Mazzotti [c], Aniello Pelella [c], Ofelia Durante [c], Eric García-Hemme [e], Antonio Di Bartolomeo [c,**]

[a] University Belhadj Bouchaib Ain Temouchent, Algeria
[b] Unit Research of Materials and Renewable Energy, Tlemcen, Algeria
[c] Department of Physics "E.R. Caianiello", University of Salerno, 84084, Fisciano, Italy
[d] University Aboubekr Belkaid, Tlemcen, Algeria
[e] Departamento de Estructura de la Materia, Física Térmica y Electrónica, Facultad de Ciencias Físicas, Universidad Complutense de Madrid, Spain

A B S T R A C T

Silicon PN junctions remain central to optoelectronic technologies due to their maturity and CMOS compatibility. We report the fabrication and comprehensive optoelectronic characterization of a silicon PN-junction photodiode demonstrating stable operation over a wide temperature range. The device exhibits excellent diode behavior, with a rectification ratio exceeding four orders of magnitude, an ideality factor close to unity above 0.3 V, and a series resistance below 100 Ω. Under white-light illumination, the photodiode shows a linear photocurrent response over broad optical power and temperature ranges, achieving an average responsivity of 0.3 A W^{-1}. We implement a machine learning framework based on an Artificial Neural Network to perform global parameter estimation, demonstrating its effectiveness in generalizing across diverse experimental datasets. Moreover, we propose a comprehensive analytical model, validated by Atlas–Silvaco simulations, that successfully captures charge transport and photogeneration mechanisms. This integrated approach, combining experimental measurements, machine learning, numerical simulations and analytical modelling, provides a robust performance benchmark and deeper insights for optimizing silicon-based optoelectronic devices.

1. Introduction

Silicon PN junction photodetectors, widely referred to as photodiodes, are foundational optoelectronic devices that convert incident photons into measurable electrical signals via the internal photoelectric effect: photons absorbed in the depletion region generate electron–hole pairs, which are separated by the built-in electric field, while carriers generated in the neutral regions can also contribute to the photocurrent if their diffusion length is sufficient to reach the depletion region, making the total photocurrent dependent on both the electric field and carrier lifetime. An external electric field under reverse-bias conditions can enhance photocharge separation and may additionally give rise to charge multiplication [1]. The intrinsic simplicity and effectiveness of this mechanism have made PN junctions a cornerstone of modern photodetection technologies.

The physical structure of a typical silicon photodiode consists of a P-type region diffused or implanted into an N-type silicon substrate (or vice-versa) to form a PN junction, creating a depletion region where photogenerated carriers are separated [2]. When the junction is reverse-biased, the depletion width increases, which reduces junction capacitance and improves high-frequency response, an essential feature for fast photodetection applications [3]. This widening of the depletion region also enhances quantum efficiency, as it increases the volume in which electron–hole pairs can be effectively collected [3]. Advanced device architectures carefully engineer doping profiles and junction depths to optimize charge collection and minimize capacitance, further improving performance in optoelectronic systems [2].

Despite the indirect bandgap, Silicon's popularity in photodetection stems from its mature fabrication processes, mechanical robustness, affordability and their electronic properties [4]. These advantages enable monolithic integration of photodetectors with complex electronic circuitry, minimizing fabrication costs and physical footprint in large-scale applications such as imaging sensors, medical diagnostics, and optical communication systems [4]. The spectral response of silicon photodiodes spans from approximately 400 nm to 1100 nm, with peak responsivity around 850–900 nm [5]. Quantum efficiencies exceeding

* Corresponding author.
** Corresponding author.
E-mail addresses: andrsessa@unisa.it (A. Sessa), adibartolomeo@unisa.it (A. Di Bartolomeo).

https://doi.org/10.1016/j.physb.2026.418479
Received 22 January 2026; Received in revised form 16 February 2026; Accepted 3 March 2026
Available online 5 March 2026

90% have been achieved in optimized PIN photodiodes, in which the intrinsic (I) layer expands the depletion region and enhances the efficiency of photocharge collection [3].

Although silicon exhibits a sharp drop in absorption beyond 900 nm, multiple strategies have emerged to extend its operational range into the near-infrared (NIR). These include surface texturing (black silicon) [6], plasmonic enhancement using metallic nanoparticles [7], and integration with quantum dots [8,9] or 2D materials [10,11]. Nanostructuring, in particular, improves light trapping by increasing the optical path length within the silicon, enhancing efficiency by up to 15% [7]. Hybrid heterojunction architectures combining silicon with functional semiconducting materials have also been widely investigated to enhance spectral sensitivity and interfacial charge separation, particularly in hybrid organic–inorganic and composite systems [12–15].

Operationally, silicon photodiodes can be used in either photovoltaic (zero bias) or photoconductive (reverse bias) modes. While the photovoltaic mode offers low noise and is ideal for energy harvesting, the photoconductive mode provides higher sensitivity, wider dynamic range and faster response times at the cost of increased dark current [8]. Dark current, caused by thermally generated carriers, can be minimized through passivation, cooling, and doping techniques, with state-of-the-art devices achieving values below 1 nA/cm^2 at room temperature [16].

To enhance sensitivity and detect extremely low light levels, silicon avalanche photodiodes (APDs) have been developed. These devices exploit internal carrier multiplication, offering gain-bandwidth products exceeding 300 GHz [17]. Recent hybrid silicon–InGaAs photodiodes extend detection beyond the 1100 nm cutoff of pure silicon while retaining its manufacturing advantages [18].

Due to their versatility, high efficiency, and low cost, silicon PN junction photodetectors have become indispensable in a wide array of applications including LiDAR, biosensing, autonomous vehicles, fiber-optic communication, and IoT devices [19]. As emerging technologies demand faster and more sensitive detection systems, ongoing research continues to optimize silicon-based photodetectors by pushing the boundaries of responsivity, bandwidth, and spectral range [5,7].

In this study, we present the fabrication and optoelectronic characterization of a silicon PN-junction photodiode over a broad temperature range. The device exhibits strong diode behavior, with an ideality factor close to unity for biases above 0.3 V, a rectification ratio exceeding four orders of magnitude, and a series resistance below 100 $\Omega\,cm^2$. As a photodetector, it demonstrates highly linear operation and stable responsivity across a wide range of optical powers and temperatures, achieving a wavelength-averaged responsivity of up to 0.3 A/W and detectivity of 1.4×10^8 Jones under white light illumination.

We show that the device current–voltage (I-V) behavior is well reproduced by a model incorporating two parallel diodes, a shunt resistance, and two series resistances. To complement traditional parameter extraction techniques, we also implement a machine learning framework based on a deep Multi-Layer Perceptron (MLP) architecture; this approach enables a robust global estimation of the diode's physical parameters, demonstrating superior versatility and generalizability compared to conventional analytical models.

Moreover, we derive a general analytical expression for the photocurrent and validate the model through comparison with Atlas–Silvaco simulations and experimental data, demonstrating good agreement.

Overall, we provide a comprehensive characterization of the Si photodevice's performance and offer deeper insight into the physical mechanisms governing its electrical and optoelectronic behavior. The originality of this work lies in the integrated use of experimental measurements, Silvaco-based simulations, both phenomenological and analytical modeling and a Machine Learning approach. The consistency among these approaches validates both the device performance and the predictive capability of our models. This integrated methodology provides unique insights into the behavior of silicon PN-junction photodiodes and highlights their potential for optimizing high-performance photodetector designs.

2. Experimental part

a. Device fabrication

The fabrication process for this silicon PN (Fig. 1) junction photodetector begins with a p-type substrate, which is then implanted with phosphorus ions to create an n-type layer and form a PN junction after rapid thermal annealing. This active area is isolated by a $10 \times 10\,mm^2$ mesa structure, created via reactive ion etching. For electrical contact, a top electrode is evaporated, consisting of a 20 nm titanium layer followed by a 200 nm aluminum layer. This electrode is shaped like an “E" to allow light penetration (see Fig. 1(a)). The final device, with its distinct mesa and top contact, is used to convert incident light into an electrical signal. A 3D schematic of the device with the “E” shaped contact is shown in Fig. 1(b).

b. Current–Voltage Characteristics as a Function of Temperature

Electrical measurements were carried out in a Lake Shore probe station under controlled temperature and at ambient pressure, using a Keithley 4200 semiconductor characterization system. Temperature of the device was controlled via the metallic chuck supporting the sample in the probe station, with precise regulation provided by a PID controller. The illumination system was made of an array of white LEDs producing a light of intensity $P = 1.75\,mW/cm^2$ on the device. The spectral emission range of the white LED comprises a prominent blue peak, around 450-470 nm, combined with a broad, yellowish-green to red hump between 500 and 700 nm.

The I-V characteristics of the fabricated diode are presented in Fig. 2 (a). A careful observation reveals the coexistence of multiple conduction mechanisms, which result in non-ideal diode behavior over certain regions. The forward bias region shows different regimes: generation–recombination current, diffusion current, and an ohmic regime dominated by series resistance [20,21].

At low forward bias, corresponding to region (a) in Fig. 2(a), the current follows an exponential law approximately proportional to $exp\left(\frac{qV}{2kT}\right)$, resulting in an ideality factor close to 2 [22]. The slope of the I-V curve suggests the dominance of recombination-mediated transport [23]. In this regime generation and recombination are governed by the Shockley–Read–Hall (SRH) mechanism that involves defect states or traps within the depletion region of the junction. At moderate forward bias (region (b)), the diffusion current becomes the main transport mechanism. In this regime, the injected minority carriers, holes in the n-region and electrons in the p-region, diffuse into the quasi-neutral regions, resulting in an exponential dependence of the current on voltage, proportional to $exp(qV/kT)$. Here, the I-V characteristic approaches the ideal Shockley behavior, with an ideality factor close to unity, indicating minority-carrier transport limited by concentration gradients, as will be explained later [24].

Finally, at sufficiently high forward currents, the exponential increase becomes limited by the series resistance. In this regime, the applied bias is partially dropped across parasitic resistive paths, including bulk resistivity of the neutral regions, contact and wire resistances, resulting in a quasi-linear dependence of current on voltage, as indicated in the high-bias portion of Fig. 2(a) [22,25].

To describe the I-V characteristics of the diode within the thermionic emission framework, it is standard practice to employ the equivalent circuit shown in Fig. 2(b), which incorporates a series resistance (R_s) and a parallel shunt resistance (R_p) [26–28].

While R_s limits the forward current at high bias, R_p accounts for leakage currents, primarily influencing the reverse-bias regime. Within

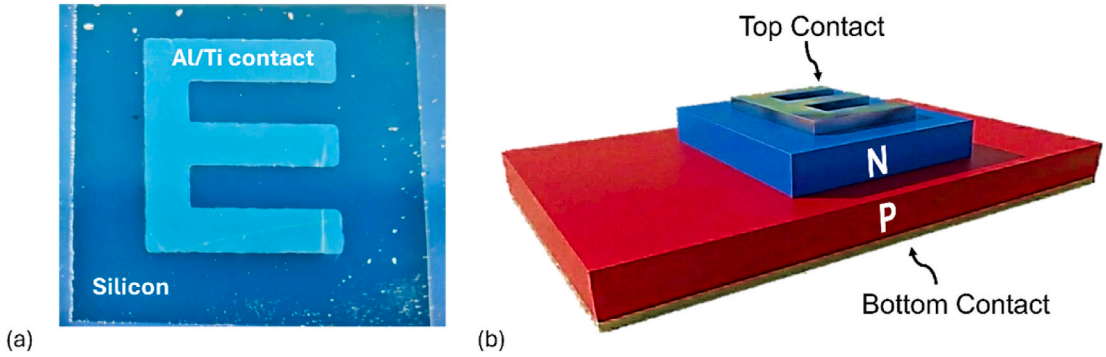

Fig. 1. (a) Optical picture of the fabricated device with the E-shaped Al/Ti contact. (b) 3D schematic of the PN Silicon photodetector (not to scale). (For interpretation of the references to colour in this figure legend, the reader is referred to the Web version of this article.)

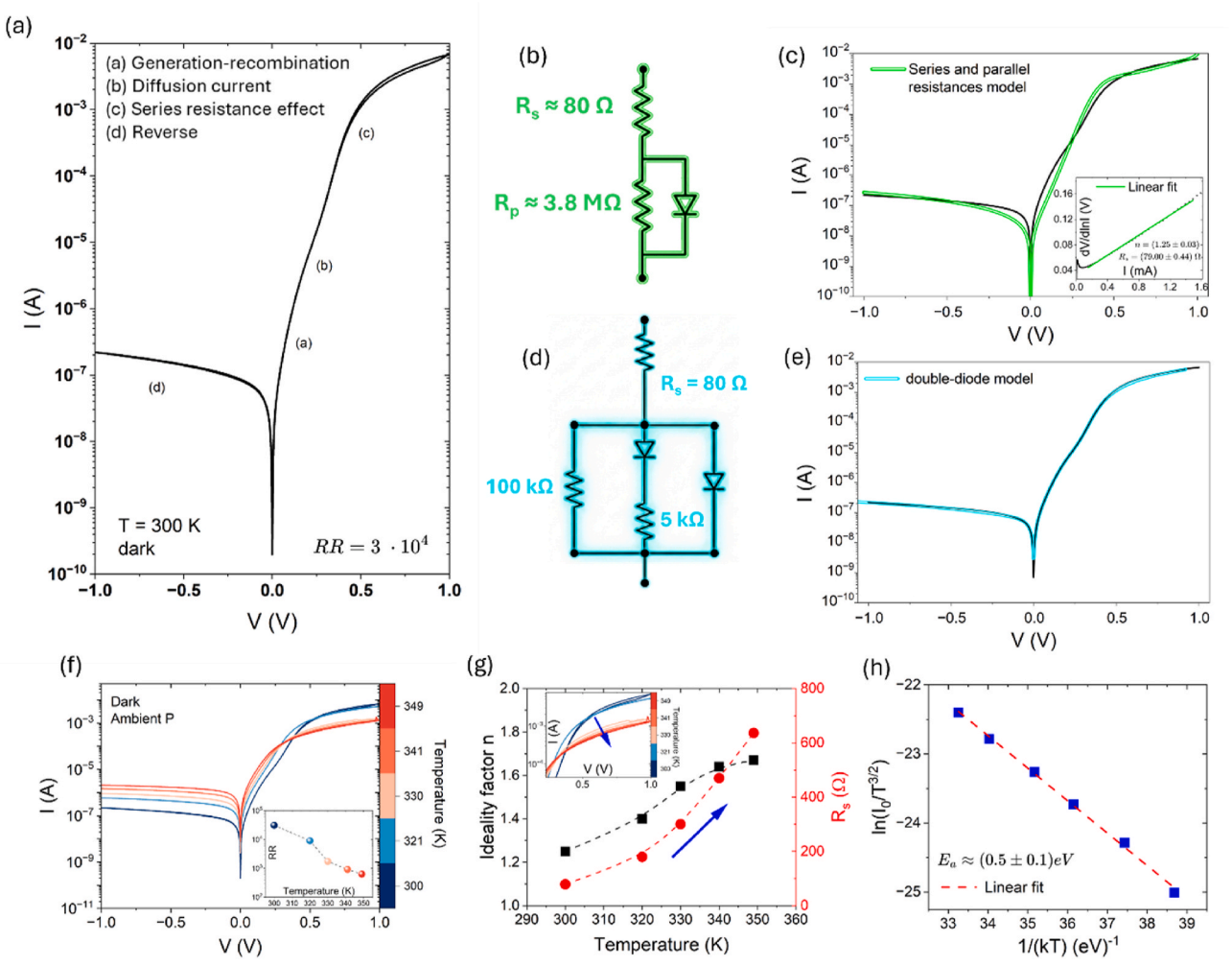

Fig. 2. **(a)** Experimental dark I-V curve (300 K) highlighting conduction regimes (recombination, diffusion, high-injection, and series resistance). **(b)** Equivalent circuit model, incorporating series (R_s) and shunt (R_p) resistances, corresponding to Eq. (1). **(c)** Fitting of the I-V characteristics using the series and parallel resistances model; inset shows the Cheung method for extracting R_s and ideality factor n. **(d)** Equivalent circuit of the double-diode model with shunt and series resistances. **(e)** Fitting of the I-V characteristics using the double-diode model. **(f)** Temperature dependence of dark I-V curves (300–349 K), showing the intensification of the series resistance effect. **(g)** Extracted R_s and n parameters vs. temperature based on the model of Eq. (1). **(h)** Arrhenius plot of the reverse saturation current, yielding an activation energy $E_a \approx 0.5\,eV$ consistent with thermal generation.

this model, the I-V behavior is expressed as:

$$I = \frac{R_p}{R_s + R_p}\left\{I_s\left[\exp\left(\frac{q(V - IR_s)}{nkT}\right) - 1\right] + \frac{V}{R_p}\right\} \quad (1)$$

The series resistance and the ideality factor, n, can be extracted from the I-V characteristics by employing a differential analysis method, commonly referred to as the Cheung method [29,30]. For high R_p, such that $\frac{R_p}{R_s+R_p} \to 1$ and $\frac{V}{R_p} \to 0$, differentiating the voltage with respect to the logarithm of the current in Eq. (1), the following linear relationship is established [31]:

$$\frac{dV}{d(lnI)} = \frac{nkT}{q} + R_s I \quad (2)$$

Thus, when $dV/d(lnI)$ is plotted against I, the result is a straight line whose slope gives R_s and whose y-intercept allows for an accurate determination of n, as shown in the inset of Fig. 2(c).

This analysis yields an effective ideality factor $n \approx 1.25$ and $R_s \approx 80\,\Omega$. This ideality factor is intermediate between the ideal diffusion limit and pure defect recombination in the space charge region, indicative of mixed recombination processes. The inclusion of a shunt resistance $R_p \approx 3.8\,M\Omega$ introduces an additional voltage-dependent leakage path. With these parameters, the forward characteristic is fitted as shown in Fig. 2(c). However, this model fails to capture the different conduction mechanisms [32,33], particularly in region (b) of Fig. 2(a). To account for the distinct mechanisms of ideal diffusion and recombination, a double-diode model, comprising a parallel combination of an ideal diode ($n = 1$) and a non-ideal diode ($n = 2$), is adopted (see Fig. S1 in the Supporting Information). In this configuration, the parallel combination of the resistor and diode in Fig. 2(b) is replaced by a parallel network of the two diodes and a resistance, all connected in series with the series resistance R_s extracted from the Cheung analysis. This modification significantly improves the fit; indeed, both the reverse region and the forward region at higher voltages ($V > 0.3\,V$) are well reproduced.

Nevertheless, the interval $0.05\,V < V < 0.3\,V$ is not accurately fitted by this model. To resolve this issue, a resistance is included in series with the non-ideal diode (see Fig. 2(d)). The additional resistance introduced in series with the non-ideal ($n = 2$) diode is attributed to interface transport mechanisms, mainly trap-assisted current channels and spatially inhomogeneous recombination paths, which become particularly relevant in the 0.05–0.3 V bias range and cannot be captured by a single global series resistance. Fig. 2(e) confirms that the proposed model accurately reproduces the full I-V curve.

The investigation into temperature dependence (from 300 to 350 K) reveals a crucial shift in device performance starting above 320 K. At elevated temperatures, the overall series resistance effect intensifies, because of the metallic behavior of the contacts and electrodes; moreover, the temperature dependence of carrier mobility in semiconductors, which typically decreases as temperature rises due to increased phonon scattering, can further increase the series resistance [34]. The enhanced effect of R_s manifests as a pronounced flattening or saturation of the forward current at higher operating temperatures (as shown in the black box in Fig. 2(f)). The performance degradation observed above 320 K suggests that further improvements could be achieved through enhanced surface passivation to suppress SRH recombination, optimization of contact materials to reduce thermally induced resistive losses, and defect-density reduction via post-fabrication annealing treatments [35].

Parameter extraction at various temperatures, carried out with the simplified model of Eq. (1) and presented in Fig. 2(g), confirms this trend: R_s systematically increases with temperature, while the ideality factor rises from 1.25 at 300 K to about 1.67 at 350 K. The latter indicates that recombination processes progressively dominate over diffusion at higher temperatures, suggesting a shift in the balance between transport mechanisms at moderate-to-high forward bias [34,36].

The thermal activation of the reverse saturation current (I_0) was also analyzed. An Arrhenius representation of $ln(I_0/T^{3/2})$ versus $1/kT$, shown in Fig. 2(h), yields an activation energy of approximately 0.5 eV. This value is close to half of the silicon bandgap ($E_g/2 \approx 0.56$), providing strong evidence that the reverse current is governed by thermal generation within the depletion region. The generation current scales with the intrinsic carrier concentration n_i, which follows $n_i \propto T^{\frac{3}{2}} exp(-E_g/2kT)$ [37]. This mechanism dominates the reverse leakage current at room temperature, exceeding the contribution of the diffusion component, which instead follows an $exp(-E_g/kT)$ dependence. The extracted activation energy, therefore, confirms that mid-gap recombination centers play the leading role in defining the leakage current in the studied device.

Fig. 3 summarizes the optoelectronic characterization of the fabricated PN junction under optical excitation. Current–voltage curves measured under illumination at different optical power densities show that the photocurrent $I_{ph} = I_{light} - I_{dark}$ increases linearly with the incident power, following $I_{ph} \propto P^{\alpha}$ with $\alpha \approx 1.00 \pm 0.01$. This behavior confirms that the device operates within the linear regime of photocarrier generation and collection, without evidence of trap filling, space-charge limitations, or gain mechanisms. As a consequence, the responsivity

$$R = \frac{I_{ph}}{P_{inc}} \quad (3)$$

remains essentially constant across the explored power range, indicating stable external quantum efficiency. In Eq. (3) , I_{ph} is the photocurrent, P_{inc} the incident power over the effective area of the device. Similar linear photocurrent response and responsivity values have been reported in silicon and III–V photodiodes operating in the low-to-moderate injection regime [38].

The built-in potential of the p-n junction facilitates the separation of optically excited charge carriers. When no external voltage is applied, the resulting potential difference across the device constitutes the fundamental mechanism of the photovoltaic effect. The schematic band-diagrams of the PN junction in the dark and under light are reported in Fig. S2 of the Supplementary Information. The short-circuit current I_{sc} exhibits a linear dependence on the optical power, while the open-circuit voltage V_{oc} shows a logarithmic scaling with incident power, as expected from the diode equation under illumination. In particular, with the following formula [39]:

$$V_{oc} = \frac{nkT}{q}\ln\frac{I_{ph}}{I_0} \quad (4)$$

the slope of V_{oc} versus $ln(P)$, an effective optical ideality factor was extracted, which was found to be larger than the value obtained from dark current–voltage analysis, i.e. $n \approx 3$. This discrepancy is consistent with previous observations in photovoltaic and photodetector devices, where the ideality factor under illumination exceeds the dark value due to additional recombination channels, particularly Shockley–Read–Hall recombination through defect states in the depletion region [40–42]. These trap-assisted recombination processes contribute more significantly under illumination and shift the balance between diffusion and recombination currents, thereby increasing the apparent ideality factor [43].

Temperature-dependent measurements of the photocurrent as a function of optical power, performed between 300 and 350 K, show that the linear relation I_{ph} persists across the entire temperature range, with no measurable deviation from unity in the power exponent. Consequently, the responsivity remains temperature-independent, confirming that the charge collection efficiency and junction electric field are not strongly affected by thermal variations within this interval. In contrast, the dark current increases significantly with temperature due to thermally activated carrier generation in the depletion region, in agreement with the extracted activation energy of approximately $E_g/2$. As a direct

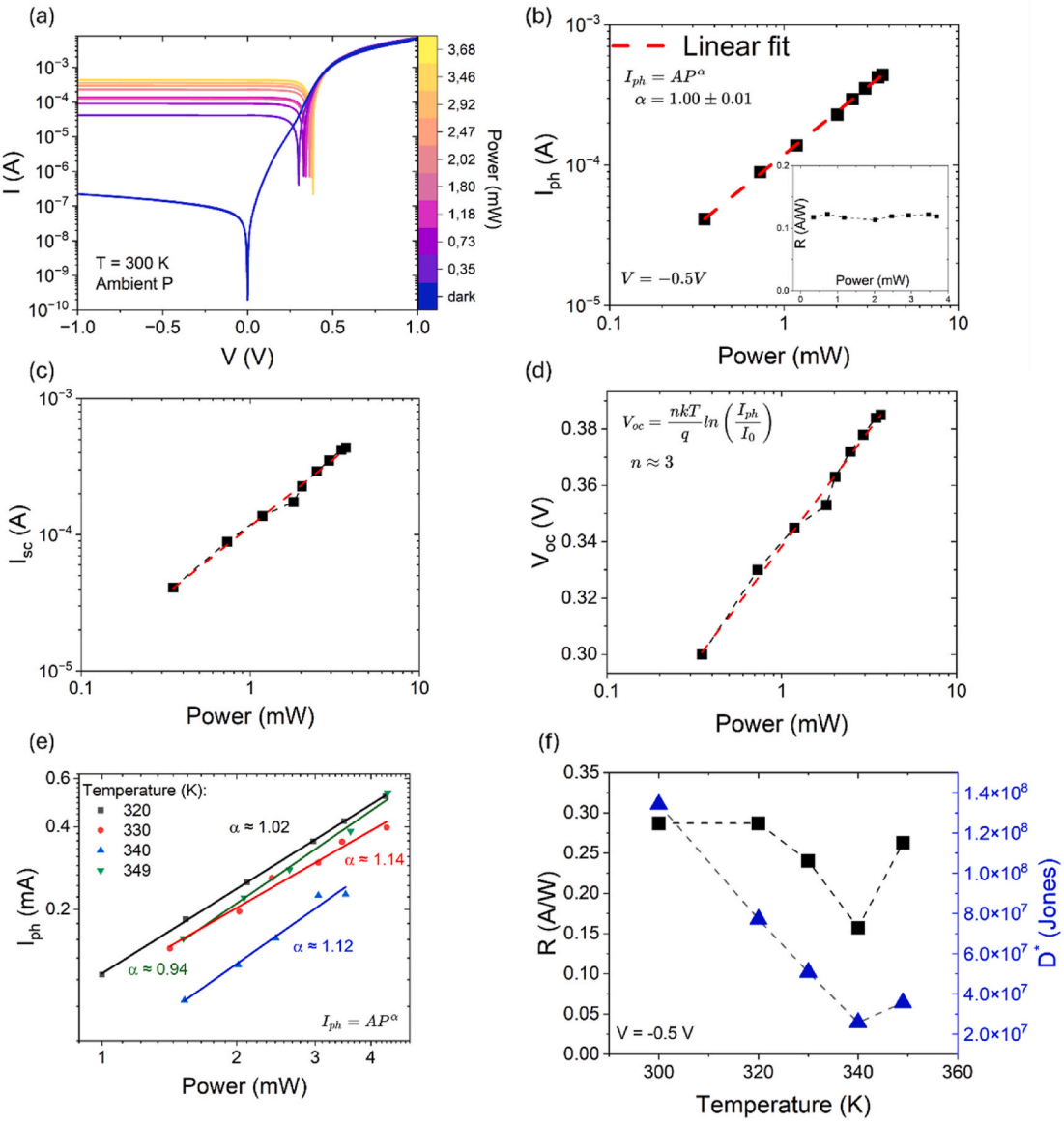

Fig. 3. **(a)** I-V curves under various incident optical powers (P). **(b)** Linear dependence of photocurrent on power (exponent $\alpha \approx 1.00$); inset confirms constant responsivity (R) vs. power. **(c)** Short-circuit current (I_{sc}) vs. optical power. **(d)** Open-circuit voltage (V_{oc}) vs. $log(P)$, showing logarithmic scaling. **(e)** Photocurrent vs. power at different temperatures, confirming the linear relation persists. **(f)** Responsivity (R) remains temperature-independent, while detectivity (D^*) decreases due to increased dark current.

consequence, the specific detectivity decreases with increasing temperature, since

$$D^* = R \cdot \sqrt{\frac{A}{2eI_{dark}}} \tag{5}$$

in the shot-noise limited regime. This trend is well established in photodiodes and photodetectors, where thermal generation dominates the noise current at elevated temperatures [44].

Overall, the optoelectronic characterization confirms that the fabricated silicon PN photodiode operates with high linearity and stable responsivity across a wide range of optical powers and temperatures. The performance is ultimately limited at elevated temperatures by thermally activated leakage currents, which reduce the detectivity despite the invariance of the responsivity.

The responsivity of a photodetector strongly depends on the incident light wavelength. Under white light, silicon absorbs only part of the spectrum efficiently, reducing the average measured responsivity compared with its peak. Optimized Si PIN photodiodes can reach ~0.4–0.6 A/W at specific wavelengths, slightly higher than the ~0.3 A/W measured under white illumination.

The responsivity reported here represents a spectral average weighted by both the emission profile of the LED source and the intrinsic wavelength-dependent absorption of silicon. The spectral region considered does not include silicon's peak responsivity, which typically occurs in the 850–900 nm range. Therefore, the quoted value corresponds to the visible band and may appear lower than the maximum responsivity measured under near-infrared illumination.

Under broad-spectrum illumination, the room temperature detectivity $D^* \sim 1.4 \times 10^8$ Jones, decreases with increasing temperature due to enhanced noise [45]. A comparative analysis between the performance of our device and state-of-the-art detectivity values for p-n junctions is provided in Table S1 of the Supplementary Information. As summarized in that Table, the specific detectivity (D*) of our silicon PN photodetector (~3.7×10^8 Jones) is comparable to reported PN devices (e.g., Refs. [46,47]) while remaining lower than most optimized PIN photodiodes (>10^{11}–10^{12} Jones) [48–50].

3. Machine learning approach to the diode characterization

To complement the conventional extraction techniques, a machine learning framework based on an Artificial Neural Network (ANN) was developed to perform global parameter estimation over the entire experimental temperature range. The electrical behavior was characterized by training a deep Multi-Layer Perceptron (MLP) architecture to map the non-linear relationship between the I-V characteristics and the physical parameters. The computational workflow was implemented in Python using the Scikit-learn library, utilizing three hidden layers with 256, 256, and 128 neurons, respectively (see Fig. 4(a)). The network was trained on a dataset of 10^4 I-V curves generated from the generalized diode equation (Eq. (1)), incorporating parasitic series and shunt resistance components. The training set was constructed by randomly varying the parameters within physically consistent ranges: ideality factor n from 1 to 2.5, saturation current I_0 from 10^{-11} to 10^{-5} A, series resistance R_s from 30 to 1000 Ω, and shunt resistance R_p from 10^5 to 10^8 Ω. Experimental data were preprocessed using a base-10 logarithmic transformation of the absolute current followed by Z-score normalization to maintain high sensitivity across multiple orders of magnitude. The optimized model employed the Adam solver and the Rectified Linear Unit (ReLU) activation function, achieving convergence with a tolerance of 10^{-8}.

The I-V characteristic at ambient temperature, processed via the Machine Learning (ML) framework, demonstrates excellent agreement with the experimental data, as illustrated in Fig. 4(b). The extracted parameters are $n = 1.68$, $R_s \approx 70\ \Omega$ and $R_p \approx 5.2\ M\Omega$. The calculated ideality factor indicates a conduction mechanism governed by a combination of an ideal ($n = 1$) and a non-ideal ($n \approx 2$) diode behaviors. Notably, the ML-derived ideality factor is slightly higher than the value obtained through Cheung's method. This discrepancy is attributed to the localized nature of the Cheung analysis, which relies on a linear fit of the auxiliary function $\frac{dV}{d(\ln I)}$. When the fitting interval is restricted or localized within the high-current regime, the Cheung method tends to overlook the global curvature, thereby underestimating the true ideality factor. Conversely, the ML approach accounts for the Shockley-Read-Hall (SRH) transport component. By extracting the saturation current from the temperature-dependent I-V curves (see Fig. S3 in the Supplementary Information), the resulting Arrhenius plot in Fig. 4(c) yields an activation energy of approximately 0.52 eV, which is in consistent agreement with experimental observations.

The primary advantage of the Machine Learning approach over traditional equivalent circuit modeling lies in its inherent versatility; it is applicable to the I-V characteristics of any electronic device, regardless of the underlying physical architecture [51], and it enables predictive performance evaluation during the design phase, thereby reducing development time and costs [52].

Unlike analytical models, which are constrained by the specific parameters and assumptions implemented within the model's equations, the ML framework provides a solution that effectively generalizes across diverse experimental datasets without requiring prior physical derivations.

4. Atlas-Silvaco simulation and analytical modeling of PN photodetectors

a. Simulation by Atlas-Silvaco

In this section, we compare the experimental I-V characteristics at room temperature with those obtained through an Atlas-Silvaco simulation and the analytical model that we detail in next session.

Fig. 5(a) illustrates the simulated structure of the studied PN

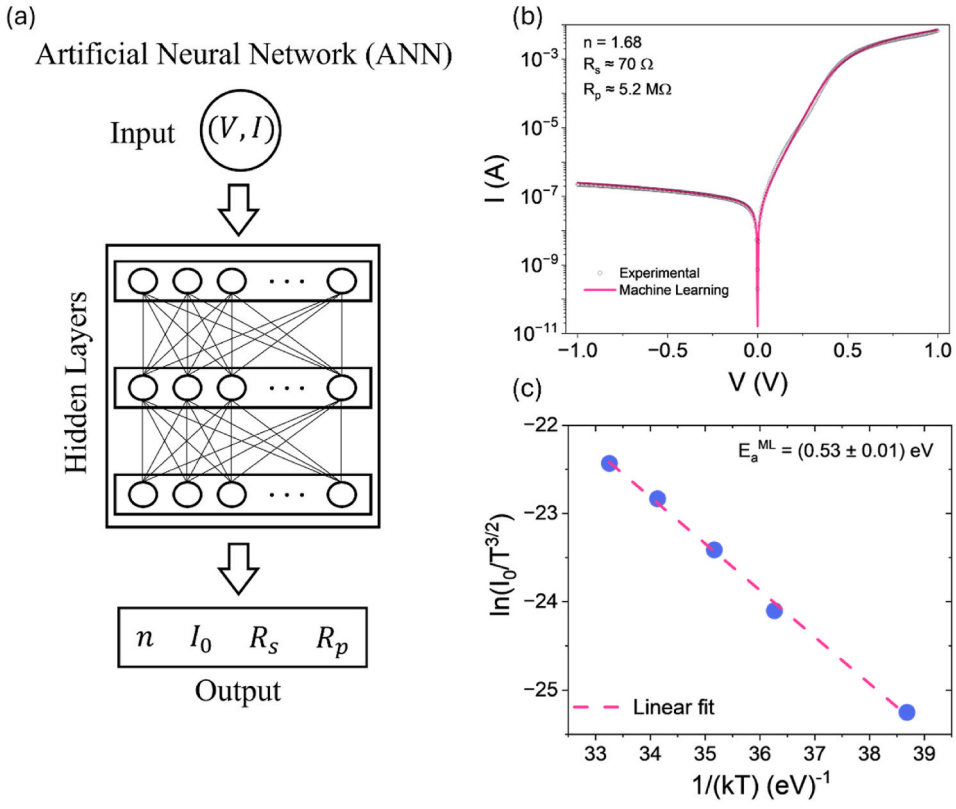

Fig. 4. **(a)** Schematic representation of the Artificial Neural Network (ANN) architecture employed for the numerical calculations. **(b)** Comparison between the experimental I-V characteristics of the PN junction and the curves reconstructed via Machine Learning (ML); the extracted parameters, including the ideality factor n, series resistance R_s, and shunt resistance R_p, are indicated. **(c)** Arrhenius plot derived from the ML-extracted saturation currents, yielding an activation energy (E_a^{ML}) of approximately 0.53 eV.

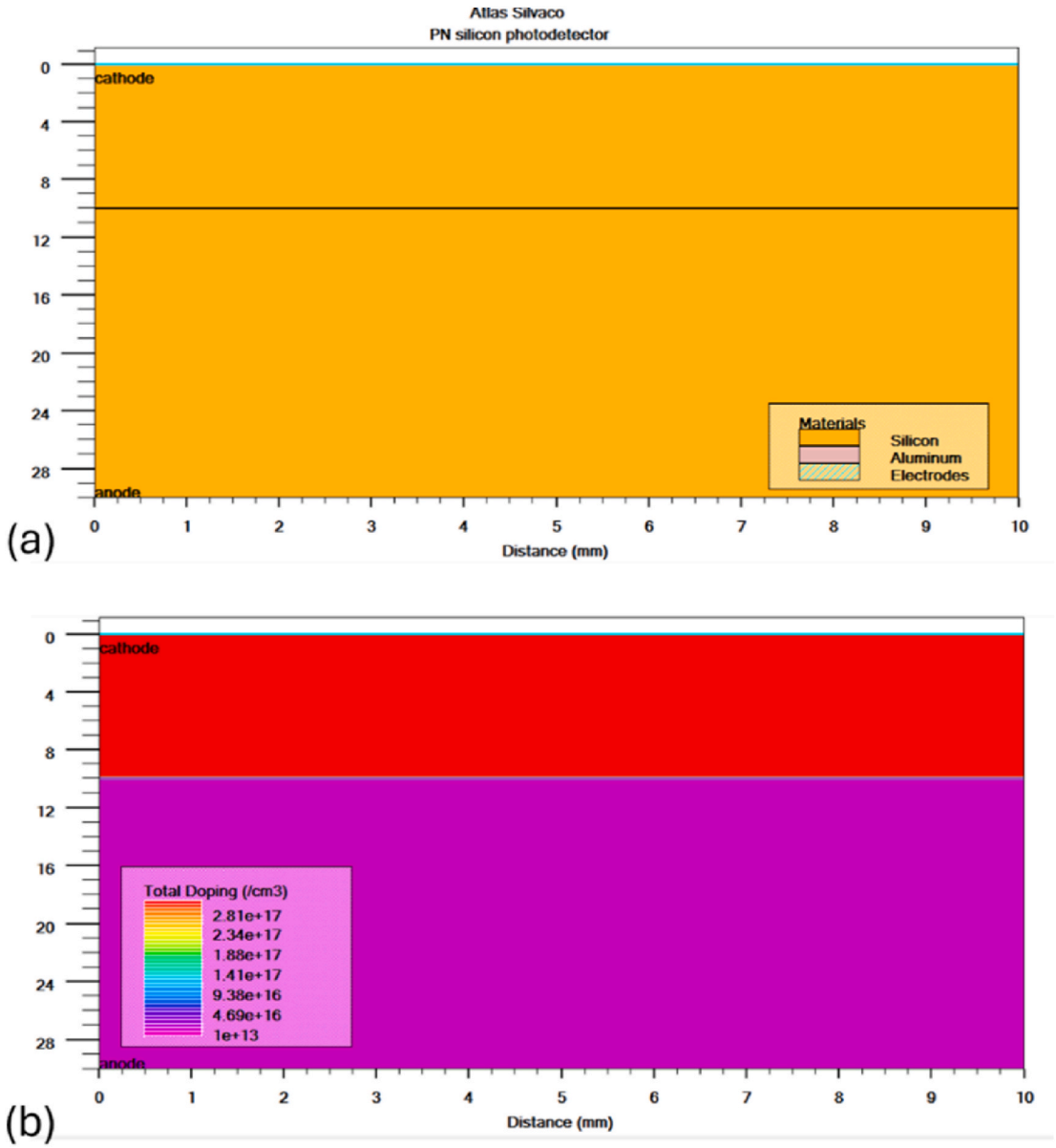

Fig. 5. **(a)** Cross section of the simulated Si PN-photodiode. **(b)** Doping profile of the simulated Si PN-photodiode.

photodetector in Atlas-Silvaco, showing a cross-sectional view of the device. Fig. 5(b) details the doping profile of the structure under study, with the n-type region in red and the p-type region in purple. The black horizontal line within the silicon marks the PN junction, the key interface for light-to-current conversion. The top and bottom layers, labeled "Electrodes," represent the Ti/Al metal contacts. The silicon PN photodiode was simulated with a set of appropriate physical models in Atlas-Silvaco device simulator to accurately capture carrier transport and recombination mechanisms. The Shockley–Read–Hall (SRH) model was enabled to account for trap-assisted recombination, while the field-dependent mobility model (FLDMOB) was used to describe carrier mobility degradation under high electric fields. The CONS-RH model was included to ensure a consistent formulation of recombination processes across different bias conditions. Device equations were solved using a combined Newton–Gummel iterative scheme to enhance numerical stability, with carrier trapping handled through the TRAP option. Convergence robustness was further improved by setting an iteration limit of 40 and a maximum of 20 trap iterations. As shown in the following, this configuration provides a reliable computational framework for analyzing the electro-optical behavior of the silicon p–n photodetector.

b. Analytical modeling

Following the insight gained through the simulation, an analytical model is proposed to obtain the I–V characteristics of silicon PN photodetector. The model is derived from the continuity equations combined with the drift–diffusion transport equations with the electrical potential obtained from the Poisson's equation self-consistently solved using the Newton–Gummel iterative method. As in the simulation, the model incorporates the Shockley–Read–Hall recombination and the field-dependent mobility. The model here proposed is general and not device-specific, as it relies solely on fundamental principles and applies to any PN junction diode.

For the sake of brevity, we present here only the final analytical expression of the current versus voltage, under illumination. A detailed derivation, including all intermediate steps and underlying assumptions, is provided in the Supplementary Information and is schematized in Fig. S4.

According to the proposed model, the I–V expression of the current in

the photodetector is the following:

$$I(V) = I_{dark}(V) - I_{photo}(V) \tag{6}$$

$$I(V) = qA\left(e^{\frac{qV}{nkT}} - 1\right)\left(\frac{n_i^2 D_p}{N_D L_p}\coth\left(\frac{t_n - x_n}{L_p}\right) + \frac{n_i^2 D_n}{N_A L_n}\coth\left(\frac{t_p - x_p}{L_n}\right)\right) - A\left[\mathrm{q}\Phi e^{-\alpha t_n}\frac{\eta\alpha\left(\alpha - \frac{1}{L_p}\right)}{\left(\alpha^2 - \frac{1}{L_p^2}\right)}e^{\frac{-(t_n - x_n)}{L_p}} + \mathrm{q}\Phi e^{-\alpha t_p}\frac{\eta\alpha\left(\alpha - \frac{1}{L_n}\right)}{\left(\alpha^2 - \frac{1}{L_n^2}\right)}e^{\frac{-(t_p - x_p)}{L_n}}\right] - \frac{qA\eta\Phi}{\alpha}\left(1 - e^{-\alpha W}\right)$$

In Eq. (6), A is the junction area, n_i the intrinsic Silicon carrier concentration, N_A and N_D the doping densities of the p- and n-regions, respectively, D_p/ D_n and L_p/ L_n are the hole/electron diffusion coefficients and lengths in the n- and p-regions, respectively, Φ is the incident photon flux, α is the absorption coefficient, η the quantum effeicieny, and x_n/ x_p with $x_n + x_p = W$ the extensions of the depletion layer in the n- and p-side.

c. Comparison of Analytical and Numerical Simulation Results with Experimental Measurements

In this section, the experimental I–V characteristics of the device are compared with results obtained from numerical simulations performed using the Atlas-Silvaco simulator and with predictions from the analytical model described in Eq. (6). The analytical model was developed in close conjunction with Silvaco TCAD simulations. The governing physical equations solved in Silvaco were used as a reference to ensure consistency with established device physics. TCAD results guided the formulation of the analytical expressions, which were then validated against Silvaco simulations over the operating range of interest. This hybrid approach enables accurate physics-based modeling while maintaining analytical simplicity.

The objective is to validate both the simulation framework and the analytical approach, demonstrating that they accurately capture the underlying physical mechanisms governing device operation.

Fig. 6(a) compares the experimental room-temperature dark I–V characteristics of the PN photodetector with those obtained from numerical simulations using the Atlas-Silvaco tool and from the analytical model. Under reverse bias, all three curves (experimental, analytical, and Atlas-Silvaco) show good agreement and exhibit a low dark current. In forward bias, both the simulation and the analytical model closely match the experimental data in the low-bias diffusion regime, with a slight underestimation at higher biases where the current becomes limited by the series resistance. Notably, the Silvaco simulation provides the closest agreement with the experimental data over the entire voltage range, thereby validating the physical mechanisms selected for modeling the device behavior.

Fig. 6(b) shows the same I-V curves under illumination. In reverse bias, all three curves, i.e., experimental, analytical, and Atlas-Silvaco, converge to a high and stable photocurrent, confirming the device's light sensitivity. The satisfactory agreement with the experimental data proves that both simulation and the analytical model capture the essential physical phenomena underlying the behavior of the photodiode under illumination, thus constituting a reliable tool for predicting the device's quantitative behavior.

5. Conclusions

In summary, we have demonstrated the fabrication and comprehensive optoelectronic characterization of a silicon PN-junction photodiode operating across a broad temperature range. The device exhibits robust diode behavior, reflected in a rectification ratio exceeding four orders of magnitude, an ideality factor close to 1 over a wide bias range, and a series resistance below 100 Ω. The entire current–voltage behavior of the diode is accurately reproduced by a phenomenological model incorporating two diodes with ideality factors of 1 and 2, along with shunt and series resistances. A key highlight of this work is the implementation of a machine learning framework based on an Artificial Neural Network, which successfully performed global parameter estimation and accurately reconstructed the I-V characteristics. This data-driven approach provided an independent validation of the physical parameters and demonstrated superior versatility in generalizing across diverse experimental conditions without the constraints of traditional analytical assumptions. As a photodetector, the device maintains a highly linear response and stable responsivity up to 0.3 A/W. We also established a general analytical expression for the photocurrent, validated by Atlas-Silvaco simulations. Collectively, this integrated methodology, combining experimental measurements, machine learning, and numerical simulations provides a powerful toolset for the precise assessment and predictive optimization of high-performance silicon-based optoelectronic devices.

CRediT authorship contribution statement

Mohammed Khaouani: Writing – original draft, Validation, Supervision, Software, Methodology, Investigation, Formal analysis, Conceptualization. **Andrea Sessa:** Writing – original draft, Validation, Software, Methodology, Investigation, Formal analysis, Data curation, Conceptualization. **Sebastiano De Stefano:** Visualization, Software, Methodology, Investigation, Data curation. **Hichem Rouigueb:** Visualization, Software, Methodology, Investigation. **Mohammed Anes Belbachir:** Visualization, Software, Methodology, Investigation. **Adolfo Mazzotti:** Visualization, Software, Methodology, Investigation. **Aniello Pelella:** Visualization, Validation, Software, Investigation. **Ofelia Durante:** Visualization, Validation, Software, Investigation. **Eric**

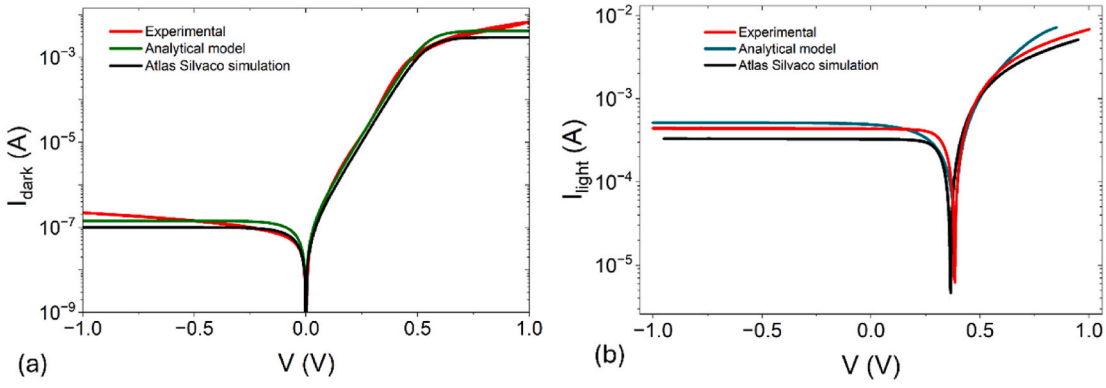

Fig. 6. Experimental, simulation and analytical I-V curve (a) in dark and (b) under light.

García-Hemme: Writing – review & editing, Validation, Supervision, Resources, Project administration, Funding acquisition, Formal analysis. **Antonio Di Bartolomeo:** Writing – review & editing, Validation, Supervision, Resources, Project administration, Funding acquisition, Data curation, Conceptualization.

Declaration of competing interest

The authors declare the following financial interests/personal relationships which may be considered as potential competing interests: Eric Garcia-Hemme reports financial support was provided by Spanish Research Agency (AEI, Ministry of Research and Innovation). Eric Garcia-Hemme reports financial support was provided by European Regional Development Fund (ERDF). Eric Garcia-Hemme reports financial support was provided by EU Recovery and Resilience Facility. Eric Garcia-Hemme reports financial support was provided by Comunidad Autonoma de Madrid, Spain. If there are other authors, they declare that they have no known competing financial interests or personal relationships that could have appeared to influence the work reported in this paper.

Acknowledgement

A.D.B. acknowledges funding from the University of Salerno through project ORSA254881.

K.M. acknowledges the “CAI de Técnicas Físicas" for the ion implantation and RTA processes.

This work was partially supported by the Spanish Research Agency (AEI, Ministry of Research and Innovation) and the European Regional Development Fund (ERDF) under grants PID2023-149369OB-C21 and PID2023-148178OB-C21.

The authors also acknowledge financial support from research grants HyperSolar (TED2021-130894B-C21) funded by the EU Recovery and Resilience Facility.

This work was partially supported by the Comunidad Autónoma de Madrid under grant PR37/24 TEC-2024/ECO-72.

Appendix A. Supplementary data

Supplementary data to this article can be found online at https://doi.org/10.1016/j.physb.2026.418479.

Data availability

Data will be made available on request.

References

[1] A. Di Bartolomeo, G. Luongo, L. Iemmo, F. Urban, F. Giubileo, Graphene–silicon schottky diodes for photodetection, IEEE Trans. Nanotechnol. 17 (2018) 1133–1137, https://doi.org/10.1109/TNANO.2018.2853798.

[2] F. Roger, I. Jonak-Auer, O. Synooka, F. Segmanovic, J. Mellin, H. Hofstaetter, F. Roger, I. Jonak-Auer, O. Synooka, F. Segmanovic, J. Mellin, H. Hofstaetter, Systematic electro-optical study of photodiodes in intrinsic material (lowly doped) with backend stack optimization, Proceedings 2 (2018), https://doi.org/10.3390/proceedings2130909.

[3] O.E. Setälä, K. Chen, T.P. Pasanen, X. Liu, B. Radfar, V. Vähänissi, H. Savin, Boron-implanted black silicon photodiode with close-to-ideal responsivity from 200 to 1000 nm, ACS Photonics 10 (2023) 1735–1741, https://doi.org/10.1021/acsphotonics.2c01984.

[4] Y. Zhang, J.Y.Y. Loh, N.P. Kherani, Facilely achieved self-biased black silicon heterojunction photodiode with broadband quantum efficiency approaching 100%, Adv. Sci. 9 (2022) 2203234 https://doi.org/10.1002/advs.202203234.

[5] S. Huang, Q. Wu, Z. Jia, X. Jin, X. Fu, H. Huang, X. Zhang, J. Yao, J. Xu, Black silicon photodetector with excellent comprehensive properties by rapid thermal annealing and hydrogenated surface passivation, Adv. Opt. Mater. 8 (2020) 1901808, https://doi.org/10.1002/adom.201901808.

[6] Z. Zhao, Z. Zhang, J. Jing, R. Gao, Z. Liao, W. Zhang, G. Liu, Y. Wang, K. Wang, C. Xue, Black silicon for near-infrared and ultraviolet photodetection: a review, APL Mater. 11 (2023) 021107, https://doi.org/10.1063/5.0133770.

[7] E. Scattolo, A. Cian, L. Petti, P. Lugli, D. Giubertoni, G. Paternoster, E. Scattolo, A. Cian, L. Petti, P. Lugli, D. Giubertoni, G. Paternoster, Near infrared efficiency enhancement of silicon photodiodes by integration of metal nanostructures supporting surface plasmon polaritrons, Sensors 23 (2023), https://doi.org/10.3390/s23020856.

[8] K.A. Lozovoy, R.M.H. Douhan, V.V. Dirko, H. Deeb, K.I. Khomyakova, O. I. Kukenov, A.S. Sokolov, N.Y. Akimenko, A.P. Kokhanenko, K.A. Lozovoy, R.M. H. Douhan, V.V. Dirko, H. Deeb, K.I. Khomyakova, O.I. Kukenov, A.S. Sokolov, N. Y. Akimenko, A.P. Kokhanenko, Silicon-based avalanche photodiodes: advancements and applications in medical imaging, Nanomaterials 13 (2023), https://doi.org/10.3390/nano13233078.

[9] A.A. Altan, Z. Berktaş, N. Kaymak, M. Yıldız, A.D. Bartolomeo, E. Orhan, Enhanced rectification of lanthanum hydroxide-doped graphene quantum dots/silicon heterostructures at cryogenic temperatures, Micro & Nano Lett. 20 (2025) e70012, https://doi.org/10.1049/mna2.70012.

[10] V. Tiwari, A. Kushwaha, N. Goel, Modeling of MoS2/Si heterostructure to study charge transfer dynamics, Nano Express 5 (2024) 025017, https://doi.org/10.1088/2632-959X/ad4a96.

[11] K. Intonti, A. Pelella, H. Neill, V. Patil, P.K. Hurley, L. Ansari, F. Gity, A. Di Bartolomeo, ReS2/Si 2D/3D vertical heterojunction as a self-powered photodiode, Appl. Phys. Lett. 125 (2024) 173505, https://doi.org/10.1063/5.0231243.

[12] R.O. Ocaya, A. Al-Ghamdi, K. Mensah-Darkwa, R.K. Gupta, W. Farooq, F. Yakuphanoglu, Organic photodetector with coumarin-adjustable photocurrent, Synth. Met. 213 (2016) 65–72, https://doi.org/10.1016/j.synthmet.2016.01.002.

[13] A. Mekki, R.O. Ocaya, A. Dere, A.A. Al-Ghamdi, K. Harrabi, F. Yakuphanoglu, New photodiodes based graphene-organic semiconductor hybrid materials, Synth. Met. 213 (2016) 47–56, https://doi.org/10.1016/j.synthmet.2015.12.026.

[14] R.O. Ocaya, A.G. Al-Sehemi, A. Al-Ghamdi, F. El-Tantawy, F. Yakuphanoglu, Organic semiconductor photosensors, J. Alloys Compd. 702 (2017) 520–530, https://doi.org/10.1016/j.jallcom.2016.12.381.

[15] A. Tataroglu, R. Ocaya, A. Dere, O. Dayan, Z. Serbetci, A.G. Al-Sehemi, M. Soylu, A. A. Al-Ghamdi, F. Yakuphanoglu, Ruthenium(II) complex based photodiode for organic electronic applications, J. Electron. Mater. 47 (2018) 828–833, https://doi.org/10.1007/s11664-017-5882-1.

[16] S.S. Li, F.A. Lindholm, Quantum yield of p–i–n photodiodes, Phys. Status Solidi A 15 (1973) 237–245, https://doi.org/10.1002/pssa.2210150126.

[17] I.S. Alirezaei, N. Andre, D. Flandre, Enhanced ultraviolet avalanche photodiode with 640-nm-Thin silicon body based on SOI technology, IEEE Trans. Electron. Dev. 67 (2020) 4641–4644, https://doi.org/10.1109/TED.2020.3017699.

[18] H. Liu, T.P. Pasanen, T.H. Fung, J. Isometsä, A. Haarahiltunen, S. Hesse, L. Werner, V. Vähänissi, H. Savin, Near-infrared germanium PIN-photodiodes with >1A/W responsivity, Light Sci. Appl. 14 (2025) 9, https://doi.org/10.1038/s41377-024-01670-4.

[19] A. Rawat, A. Ahamed, C. Bartolo-Perez, A.S. Mayet, L.N. McPhillips, M.S. Islam, Design and fabrication of high-efficiency, low-power, and low-leakage Si-Avalanche photodiodes for low-light sensing, ACS Photonics 10 (2023) 1416–1423, https://doi.org/10.1021/acsphotonics.3c00026.

[20] p-n junctions, in: Phys. Semicond. Devices, John Wiley & Sons, Ltd, 2006, pp. 77–133, https://doi.org/10.1002/9780470068328.ch2.

[21] A. Di Bartolomeo, K. Intonti, L. Peluso, R. Di Marco, G. Vocca, F. Romeo, F. Giubileo, A. Grillo, E. Orhan, Metal-semiconductor Schottky diode with Landauer's formalism, Nano Express 6 (2025) 022501, https://doi.org/10.1088/2632-959x/ade460.

[22] O. Almora, K.T. Cho, S. Aghazada, I. Zimmermann, G.J. Matt, C.J. Brabec, M. K. Nazeeruddin, G. Garcia-Belmonte, Discerning recombination mechanisms and ideality factors through impedance analysis of high-efficiency perovskite solar cells, Nano Energy 48 (2018) 63–72, https://doi.org/10.1016/j.nanoen.2018.03.042.

[23] J. Park, C. Yu, S. Min, J.-I. Shim, D.-S. Shin, Extracting the inherent ideality factor of a diode from electrical current–voltage characteristics, Electron. Lett. 59 (2023) e13046, https://doi.org/10.1049/ell2.13046.

[24] Z. Wang, Z. Cheng, A.E. Delahoy, K.K. Chin, A study of light-sensitive ideality factor and voltage-dependent carrier collection of CdTe solar cells in forward bias, IEEE J. Photovoltaics 3 (2013) 843–851, https://doi.org/10.1109/JPHOTOV.2013.2247095.

[25] O.Ya. Olikh, Relationship between the ideality factor and the iron concentration in silicon solar cells, Superlattice. Microst. 136 (2019) 106309, https://doi.org/10.1016/j.spmi.2019.106309.

[26] A.D. Bartolomeo, G. Luongo, L. Iemmo, F. Urban, F. Giubileo, Graphene–silicon schottky diodes for photodetection, IEEE Trans. Nanotechnol. 17 (2018) 1133–1137, https://doi.org/10.1109/TNANO.2018.2853798.

[27] A. Pelella, A. Grillo, E. Faella, G. Luongo, M.B. Askari, A. Di Bartolomeo, Graphene–silicon device for visible and infrared photodetection, ACS Appl. Mater. Interfaces 13 (2021) 47895–47903, https://doi.org/10.1021/acsami.1c12050.

[28] S. Bitter, P. Schlupp, H. von Wenckstern, M. Grundmann, Vital role of oxygen for the formation of highly rectifying schottky barrier diodes on amorphous zinc–tin–oxide with various cation compositions, ACS Appl. Mater. Interfaces 9 (2017) 26574–26581, https://doi.org/10.1021/acsami.7b06836.

[29] K.P. Cheung, J.P. Campbell, A physics-based simple series resistance extraction methodology, in: 11th Int. Workshop Junction Technol. IWJT, 2011, pp. 104–107, https://doi.org/10.1109/IWJT.2011.5970011.

[30] G. Luongo, A. Di Bartolomeo, F. Giubileo, C.A. Chavarin, C. Wenger, Electronic properties of graphene/p-silicon Schottky junction, J. Phys. Appl. Phys. 51 (2018) 255305, https://doi.org/10.1088/1361-6463/aac562.

[31] A. Di Bartolomeo, F. Giubileo, G. Luongo, L. Iemmo, N. Martucciello, G. Niu, M. Fraschke, O. Skibitzki, T. Schroeder, G. Lupina, Tunable Schottky barrier and

high responsivity in graphene/Si-nanotip optoelectronic device, 2D Mater. 4 (2016) 015024, https://doi.org/10.1088/2053-1583/4/1/015024.
[32] A. Tataroğlu, Ş. Altındal, The analysis of the series resistance and interface states of MIS Schottky diodes at high temperatures using *I–V* characteristics, J. Alloys Compd. 484 (2009) 405–409, https://doi.org/10.1016/j.jallcom.2009.04.119.
[33] C.P.Y. Wong, Gaussian thermionic emission model for analysis of AuMoS2 Schottky-BarrierDevices, Phys. Rev. Appl. 14 (2020), https://doi.org/10.1103/PhysRevApplied.14.054027.
[34] I.S. Amiri, F.M.A.M. Houssien, A.N.Z. Rashed, A.E.-N.A. Mohammed, Temperature effects on characteristics and performance of near-infrared wide bandwidth for different avalanche photodiodes structures, Results Phys. 14 (2019) 102399, https://doi.org/10.1016/j.rinp.2019.102399.
[35] J. Prabket, I. Srithanachai, S. Ueamanapong, A. Poyai, W. Titiroongruang, S. Niemcharoen, P.P. Yupapin, An improvement of electrical characteristics of P-N diode by X-ray irradiation method, Sci. Res. Essays 7 (2012) 1230–1236, https://doi.org/10.5897/SRE11.2076.
[36] Z. Hu, K. Nomoto, B. Song, M. Zhu, M. Qi, M. Pan, X. Gao, V. Protasenko, D. Jena, H.G. Xing, Near Unity ideality factor and shockley-read-hall lifetime in GaN-on-GaN p-n diodes with avalanche breakdown, Appl. Phys. Lett. 107 (2015) 243501, https://doi.org/10.1063/1.4937436.
[37] M. Razeghi, Semiconductor p-n and metal-semiconductor junctions, in: M. Razeghi (Ed.), Fundam. Solid State Eng., Springer International Publishing, Cham, 2019, pp. 319–363, https://doi.org/10.1007/978-3-319-75708-7_9.
[38] A. Rogalski, Infrared detectors: an overview, Infrared Phys. Technol. 43 (2002) 187–210, https://doi.org/10.1016/S1350-4495(02)00140-8.
[39] M. Auf der Maur, G. Moses, J.M. Gordon, X. Huang, Y. Zhao, E.A. Katz, Temperature and intensity dependence of the open-circuit voltage of InGaN/GaN multi-quantum well solar cells, Sol. Energy Mater. Sol. Cells 230 (2021) 111253, https://doi.org/10.1016/j.solmat.2021.111253.
[40] W. Tress, M. Yavari, K. Domanski, P. Yadav, B. Niesen, J.P.C. Baena, A. Hagfeldt, M. Graetzel, Interpretation and evolution of open-circuit voltage, recombination, ideality factor and subgap defect states during reversible light-soaking and irreversible degradation of perovskite solar cells, Energy Environ. Sci. 11 (2018) 151–165, https://doi.org/10.1039/C7EE02415K.
[41] T. Kirchartz, U. Rau, What makes a good solar cell? Adv. Energy Mater. 8 (2018) 1703385 https://doi.org/10.1002/aenm.201703385.
[42] C. Sah, R.N. Noyce, W. Shockley, Carrier generation and recombination in P-N junctions and P-N junction characteristics, Proc. IRE 45 (1957) 1228–1243, https://doi.org/10.1109/JRPROC.1957.278528.
[43] M. Neukom, S. Züfle, S. Jenatsch, B. Ruhstaller, Opto-electronic characterization of third-generation solar cells, Sci. Technol. Adv. Mater. (2018). https://www.tandfonline.com/doi/abs/10.1080/14686996.2018.1442091. (Accessed 6 October 2025).
[44] A. Rogalski, Progress in focal plane array technologies, Prog. Quant. Electron. 36 (2012) 342–473, https://doi.org/10.1016/j.pquantelec.2012.07.001.
[45] A. Koçyiğit, A. Sarılmaz, T. Öztürk, F. Ozel, M. Yıldırım, A Au/CuNiCoS4/p-Si photodiode: electrical and morphological characterization, Beilstein J. Nanotechnol. 12 (2021) 984–994, https://doi.org/10.3762/bjnano.12.74.
[46] A.V. Shevlyagin, D.L. Goroshko, E.A. Chusovitin, K.N. Galkin, N.G. Galkin, A. K. Gutakovskii, Enhancement of the Si p-n diode NIR photoresponse by embedding β-FeSi2 nanocrystallites, Sci. Rep. 5 (2015) 14795, https://doi.org/10.1038/srep14795.
[47] M. Wang, E. García-Hemme, Y. Berencén, R. Hübner, Y. Xie, L. Rebohle, C. Xu, H. Schneider, M. Helm, S. Zhou, Silicon-based intermediate-band infrared photodetector realized by Te hyperdoping, Adv. Opt. Mater. 9 (2021) 2101798, https://doi.org/10.1002/adom.202101798.
[48] O. Surucu, D.E. Yıldız, M. Yıldırım, A study on the dark and illuminated operation of Al/Si3N4/p-Si Schottky photodiodes: optoelectronic insights, Appl. Phys. A 130 (2024) 103, https://doi.org/10.1007/s00339-024-07284-2.
[49] M. Andelkovic, Kh.Yu. Rakhimov, A. Chaves, G.R. Berdiyorov, M.V. Milošević, Wave-packet propagation in a graphene geometric diode, Phys. E Low-Dimens. Syst. Nanostructures 147 (2023) 115607, https://doi.org/10.1016/j.physe.2022.115607.
[50] B. H, K.P. S, K.N. N.U, Low temperature-processed ZnO thin films for p–n junction-based visible-blind ultraviolet photodetectors, RSC Adv. 8 (2018) 37365–37374, https://doi.org/10.1039/C8RA07312K.
[51] R.O. Ocaya, A.A. Akinyelu, A.G. Al-Sehemi, A. Dere, A.A. Al-Ghamdi, F. Yakuphanoğlu, Machine learning models for efficient characterization of Schottky barrier photodiode internal parameters, Sci. Rep. 13 (2023) 13990, https://doi.org/10.1038/s41598-023-41111-7.
[52] B. Ersöz, A. Öter, Z. Berktaş, H.İ. Bülbül, A. Di Bartolomeo, Ş. Sağıroğlu, E. Orhan, Artificial intelligence-driven data generation for temperature-dependent current–voltage characteristics of diodes, FlatChem 51 (2025) 100847, https://doi.org/10.1016/j.flatc.2025.100847.